Peer-reviewed version available at Elsevier Computers in Biology and Medicine 2018; doi:10.1016/j.compbiomed.2018.03.015

3-D SEGMENTATION OF LUNG NODULES USING HYBRID LEVEL SETS

Hina Shakir[a,*], Tariq Mairaj Rasool Khan[b], Haroon Rasheed[a]

[a] *Department of Electrical Engineering, Bahria University, 13-National Stadium Road Karachi, 75620, Pakistan*
[b] *Department of Electrical and Power Engineering, Pakistan Navy Engineering College, National University of Science and Technology, Karachi, Pakistan*

Abstract

Lung nodule segmentation in CT images and its subsequent volume analysis can help determine the malignancy status of a lung nodule. While several efficient segmentation schemes have been proposed, only a few studies evaluated the segmentation's performance for large nodules. In this research, we contribute a semi-automatic system which is capable of performing robust 3-D segmentations on both small and large nodules with good accuracy. The target CT volume is de-noised with an anisotropic diffusion filter and a region of interest is selected around the target nodule on a reference slice. The proposed model performs nodule segmentation by incorporating a mean intensity based threshold in Geodesic Active Contour model in level sets. We also devise an adaptive technique using image intensity histogram to estimate the desired mean intensity of the nodule. The proposed system is validated on both lung nodules and phantoms collected from publicly available diverse databases. Quantitative and visual comparative analysis of the proposed work with the Chan-Vese algorithm and statistic active contour model of 3D Slicer platform is also presented. The resulting mean spatial overlap between segmented nodules and reference nodules is 0.855, the mean volume bias is 0.10 ± 0.2 ml and the algorithm repeatability is 0.060 ml. The achieved results suggest that the proposed method can be used for volume estimations of small as well as large-sized nodules.

Keywords: hybrid level-sets, active contours, nodule segmentation, hybrid deformable model

1. Introduction

Lung cancer is a leading cause of cancer-related deaths among males and females worldwide [1]. It often appears as opaque lesions in the lungs, referred to as lung nodules. The symptoms of lung

*I am corresponding author
Email addresses: hinashakir.bukc@bahria.edu.pk (Hina Shakir), khan.tariq@nust.pnec.pk (Tariq Mairaj Rasool Khan), haroonrasheed.bukc@bahria.edu.pk (Haroon Rasheed)

cancer typically manifest at an advanced stage, which makes the treatment least likely to work. A 5- year survival rate for detection in the initial stages is approximately 54 % whereas, for advanced stages it is only 4 %[2]. Thus, early detection and treatment of lung nodules can help increase the life expectancy of lung cancer patients.

Compelling studies by Field et al.[3] and Nanda et al.[4] have shown that Computed tomography (CT) is more sensitive towards nodule detection than the chest radiography, and is frequently used for detection of lung cancer. Currently, Response Evaluation Criteria In Solid Tumors (RECIST) is a vastly adopted protocol which uses the maximum diameter of the tumor as a key parameter to measure the nodule response. While RECIST is simple to follow, there is variability in intraobserver and interobserver RECIST measures due to a different interpretation of manually measured data. The problem with the RECIST protocol has been effectively addressed with volume estimation, which takes into account the overall changes in nodules [5]. The nodule volume is measured after its segmentation, hence correct nodule segmentation plays a crucial role in volumetric assessment and diagnostic tests.

In this article, we present a robust and accurate 3-D segmentation scheme for lung nodules of varying sizes in CT images to aid the clinicians for correct volumetric assessment. The segmentation process is initialized with a 3-D region of interest (ROI) drawn around the target nodule on a reference CT slice. Followed by the initialization, ROI is denoised using an anisotropic diffusion filter. The location of the nodule is identified by applying Geodesic Active Contour(GAC) model, a parametric deformable model to the denoised ROI. In order to prevent the boundary leakage of the evolved contour, a mean gray-value threshold value is introduced within the GAC model. The proposed model executes in level sets. Consequently, an active contour is evolved around the nodule leading to accurate segmentation. Moreover, an adaptive technique to estimate the desired mean intensity of the nodule is also devised. This process enables robust segmentation of nodules irrespective of the sizes. Further, any anatomical structure within the region of interest is automatically detected and removed. After the completion of the segmentation process, nodule volume is computed.

The presented method is evaluated by segmenting 72 nodules from 50 CT volumes obtained from diverse databases and is further assessed in terms of bias, spatial overlap, and repeatability. A qualitative and quantitative comparison of the presented work with the Chan-Vese algorithm and statistic active contour model of 3D Slicer platform is also shown.

Rest of the paper is organized as follows. In section 2, related work and contribution of the

proposed system are discussed. The proposed hybrid segmentation system is explained in section 3. Experiments' results and discussion on the system's performance are presented in section 4 and section 5 respectively. We draw the conclusion of our proposed research work in section 6.

2. Related Work

Among contemporary 3-D segmentation models, deformable models have been actively researched for medical image segmentation [6]. These models evolve surfaces within an image whose movement is influenced by internal and external forces. The internal forces are applied from within the curve, while the external forces are calculated from the image region data. Deformable models are often referred to as active contours, snakes, balloons and deformable surfaces. For computational convenience, these models have commonly been executed within the level set framework. In the literature surveyed, deformable models are also investigated for lung nodules segmentation. Kawata et al.[7] proposed a 3-D deformable model approach to perform nodule segmentation. El-Baz et al.[8] segmented the lung nodules in 3-D using variational level sets. Yoo et al.[9] presented a segmentation technique for semi-solid nodules by introducing a multiphase level sets framework. Way et al.[10] proposed an explicit active contour method which used 3D gradient and curvature to penalize contours and to minimize the energy function. K. Chen et al.[11] incorporated a new fuzzy speed function in the active contour model to evolve the contour. The speed function computation was based on the intensity feature and local shape index. Bin Li at al.[12] used adaptive local region energy embedded in the active contour model to segment juxta-vascular nodules. In a broader sense, all deformable models utilize either region-based or boundary-based information in the image to evolve the curve around an object. However, boundary-based segmentation exhibit poor convergence in case of noisy or weak boundaries [13]. On the contrary, the region-based active contour model can suffer over-segmentation or under-segmentation if the object is not correctly defined by the region properties [14]. Hybrid techniques integrating good features of the region as well as the boundary of the nodule offer good potential for the development of efficient and accurate segmentation algorithms.

2.1. Contribution of the proposed work

The motivation for the presented work is to increase the accuracy of lung nodule segmentation in 3-D independently, of the nodule's shape and size with minimum assumptions and inputs required. Among many semi-automatic 3-D algorithms that are proposed in the literature, Kostis et al.[15],

Peer-reviewed version available at Elsevier Computers in Biology and Medicine 2018; doi:10.1016/j.compbiomed.2018.03.015

Okada et al.[16], Diciotti et al.[17], Kuhnigk et al.[18], Moltz et al.[19], Bendtsen et al.[20] and Messay et al.[21] proposed solutions to tackle the complexities due to weak edges, intensity inhomogeneity and anatomical attachments with the lung nodule. While the aforesaid algorithms contribute to the state of the art, Kostis et al., Okada et al. and Diciotti et al. in [15-17] directed their efforts towards small nodule segmentation whereas, Kuhnigk et al., Moltz et al., Bendtsen et al. and Messay et al. in [18-21] proposed solutions to segment small as well as large nodules at the expense of several assumptions and user feedback. In contrast, our segmentation model is capable of extracting nodule contours of any sizes and shapes efficiently with a simple selection of the region of interest on the CT image.

The proposed hybrid approach exploits the gradient information to precisely identify the location of nodule whereas, the mean intensity information of nodule prevents contour leakage from the nodule boundaries. This simple yet intuitive mechanism ensures robust 3-D segmentation of the lung nodules of varying shapes and sizes with good accuracy.

3. Proposed hybrid segmentation system

The mathematical model and algorithm of our proposed segmentation system are explained in the following sub-sections. Subsequently, we discuss the architecture and validation databases of our segmentation system.

3.1. Mathematical Model

We describe $F(x) : [0; 1] \rightarrow \Re^2$ as a parameterized closed planar curve and $I : [0; a] \times [0; b] \rightarrow \Re^+$ a given input image in which the contour of the object needs to be detected. The Geodesic Active Contour (GAC) model which is a boundary-based segmentation method detects the contour by finding a minimum length of the evolving curve around object. This is achieved by minimizing the energy of the curve $F(x)$ in a Riemannian space as follows [22] :

$$E(F) = \int g(F(x))|F'(x)|dx \tag{1}$$

Here g is a decreasing edge detection function defined with respect to Riemannian space. The curve is deformed towards local minima by minimizing the curve evolution flow to 0 using steepest descent method. Curve evolution flow is a partial differential equation (PDE), obtained by computing Euler-Lagrange of Eq. (1) with gradient-descent method as follows:

$$\frac{\partial F(t)}{\partial t} = g(I)k\overrightarrow{a_n} - (\nabla g.\overrightarrow{a_n})\overrightarrow{a_n} \tag{2}$$

Here k denotes the curvature and $\overrightarrow{a_n}$ represents the unit inward vector normal to the curve $F(x,t)$. We use the term contour in this paper interchangeably for curve in 2-D and surface in 3-D. The segmentation PDEs are usually solved using a well-known framework called level sets [23], [24], [25] and [26]. The level set formulation enables implicit handling of topological changes i.e. merging and splitting of the contours and offers stability and accuracy in numerical computation. A level set function is defined as an evolving active contour $F \subset \Omega$ represented by the zero level set of a Lipschitz function $\phi : \Omega \rightarrow \Re^2$. A zero level set is visualized as a hypersurface of level set function ϕ representing the active contour F such that $F = \{x|\phi(x) = 0\}$. Evolution of planar curve F and deformation of level set function ϕ are obtained using the following PDEs respectively:

$$\frac{\partial F(t)}{\partial t} = \beta(\overrightarrow{a_N}) \tag{3}$$

$$\frac{\partial \phi}{\partial t} = \beta|\nabla\phi| \tag{4}$$

Here β is a function computed on the level sets. Caselles et al. employed Eq. (3) and Eq. (4) to embed curve evolution PDE of F in Eq. (2) in level set formulation ϕ as follows:

$$\frac{\partial \phi}{\partial t} = g(I) \mid \nabla\phi \mid k + \nabla g(I).\nabla\phi \tag{5}$$

Here the value of curvature k is computed as:

$$k = \frac{\nabla\phi}{\mid \nabla\phi \mid} \tag{6}$$

An extra contracting /expanding term is added to Eq. (5) to increase the speed of convergence as follows in [27]:

$$\frac{\partial \phi}{\partial t} = g(I) \mid \nabla\phi \mid k + \nabla g(I).\nabla\phi + vg(I) \tag{7}$$

Here v is the Lagrange multiplier. The first term in the above PDE represents mean curvature flow-weighted by edge detection function whereas, the second term attracts the contours to the boundaries of objects i.e. towards image with a high gradient. The third term is an additional gradient-based stopping function for fast convergence. The active contour model by Caselles et al. in Eq. (7) shows leakage of contours in case of weak and/or noisy object boundaries, leading to wrong convergence. To tackle this problem, we propose to introduce a new stopping function $(I - I_{mean})$ based on the mean intensity I_{mean} of the nodule in the curve evolution PDE instead of gradient term. The curve evolution PDE of Eq. (5) after introducing the new stopping function is formulated as follows:

Preprints (www.preprints.org) | NOT PEER-REVIEWED | Posted: 5 April 2019 doi:10.20944/preprints201904.0069.v1

Peer-reviewed version available at Elsevier Computers in Biology and Medicine 2018; doi:10.1016/j.compbiomed.2018.03.015

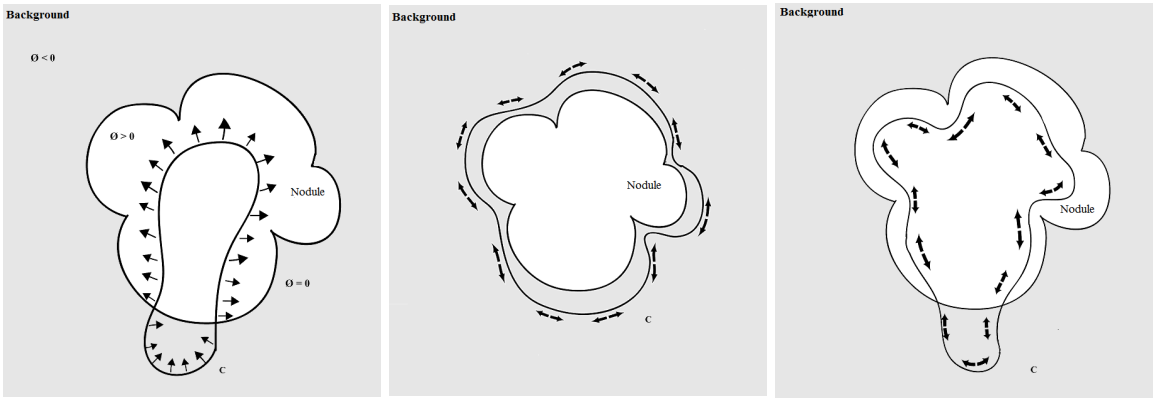

(a) (b) (c)

Figure 1: Curve evolution of the proposed method with (a) correct I_{mean} (b) I_{mean} set lower than desired (c) I_{mean} set higher than desired

$$\frac{\partial \phi}{\partial t} = bg(I) \mid \nabla \phi \mid k + b\nabla g(I).\nabla \phi + c(I - I_{mean}) \mid \nabla \phi \mid \tag{8}$$

Here b and c are pre-defined weights to balance the equation reducing $\frac{\partial \phi}{\partial t}$ to 0 for steady-state solution. For computational convenience, a zero level set is represented by the signed distance function (SDF) i.e. $|\nabla \phi| = 1$. Thus, using the SDF property and substituting value of k in Eq. (8), the foregoing equation is simplified as:

$$\phi_t = bdiv(g(I)\nabla \phi) + c(I - I_{mean}) \tag{9}$$

The simplified model presented in Eq. (9) is the proposed hybrid model for lung nodules segmentation where curve evolution flow term $\frac{\partial \phi}{\partial t}$ is denoted by ϕ_t . Value of g is computed using a Gaussian kernel with variance σ, whereas the optimal value of σ is found out through experiments to avoid over(under) segmentation.

The proposed stopping function $(I - I_{mean})$ attaches the contour to nodule boundaries for gray- values above I_{mean} . It counters the boundary leakage problem by contracting/expanding the contour around boundary based on the prior estimated boundary gray-levels threshold enabling fast convergence. The forces applied to the evolving contour by this new stopping function act normal to the surface. Figure 1(a) displays the contour evolution using the hybrid method with a correct gray-level threshold. Two cases of incorrect contour formation due to inappropriate selection of mean gray-level threshold are illustrated in Figure 1(b) and Figure 1(c) respectively. Evidently,

a good estimation of I_{mean} is essential for successful segmentation through the presented hybrid model.

3.1.1. Adaptive technique for I_{mean} calculation

In order to calculate the mean gray-value for correct segmentation, the voxel intensity distribution patterns of lung nodules from test data were investigated. The nodule gray-values were obtained by drawing a region of interest (ROI) around each target nodule on the reference CT slice followed by calculation of its ROI properties. The obtained voxels' gray levels were consistent within the range of 0 to 2000 in signed 16-bit format. Based on the gray-values, nodules histograms were plotted and analyzed. A bi-modal frequency trend was observed across all the histograms. We display our results for 10 bins for three sample nodules with different radio-densities in Figure 2. Moreover, the mean gray-values I_n of these three nodules and their respective occurrence frequencies f_n from Figure 2 are tabulated in Table 1. In order to obtain the desired approximation, we attempted to identify the bin-wise gray-values within nodule intensity data. This process was repeated for several nodules to achieve befitting results. We concluded that the last 30 % bins of the total N bins contain higher intensity values, that approximately represent the bright nodule core as well as the boundary intensity values. Therefore, I_{mean} is obtained by computing the weighted mean of the largest 30 % gray-values from gray-level histogram of a lung nodule. A constant gray-value I_0 is introduced to strengthen the I_{mean} estimation. Adaptively, we compute the value of I_{mean} as follows:

$$I_{mean} \approx \frac{\sum_m^N (I_n f_n)}{\sum_m^N (f_n)} + I_o \tag{10}$$

Here m is the bin index from upper 30 % of the total N bins. Numerically, the algorithm employs an iterative scheme to approximate the curve evolution PDE around lung nodule. The level set function ϕ takes positive and negative values outside and inside the contour C respectively. We assume that $\phi_t(k+1)$ and $\phi_t(k)$ denote the value of $\phi_t(k)$ at $(k+1)^{th}$ and k^{th} iteration respectively. The hybrid model PDE of Eq.(9) is optimized using the steepest descent gradient method as follows:

$$\phi_t(k+1) = \phi_t(k) + \triangle t div(g(I)\nabla\phi) + c(I - I_{mean}) \tag{11}$$

Here $\triangle t$ defines the predefined update step size. The value of $\phi_t(k)$ is numerically updated at each iteration undertaking the step-wise procedure explained in Algorithm 1.

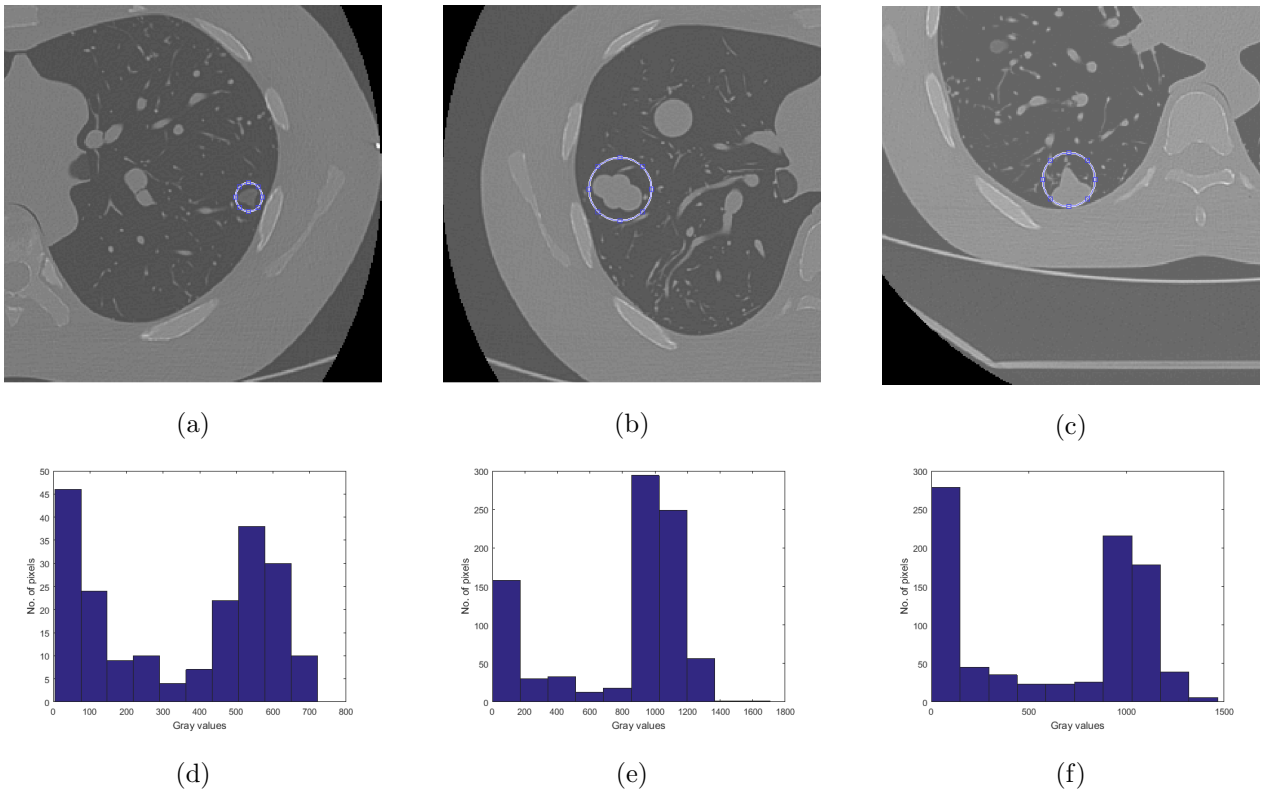

Figure 2: (a), (b), (c) show nodules within the ROI with mean radiodensity of -630 HU,-10 HU, and 100 HU respectively and (d), (e), (f) are gray-values histograms of (a), (b), (c) respectively

3.2. 3-D Segmentation Algorithm

Periodic re-initialization of ϕ to the SDF in Step 1 and Step 3 helps avoid any irregularities which can develop during the level set evolution [28]. The value of $\phi_t(k+1)$ in Step 4 is computed using Additive Operator Splitting (AOS) method [29] which is an unconditionally stable finite difference method for GAC problem. AOS scheme enables fast convergence of the algorithm in a few iterations.

3.3. System Architecture

Prior to segmentation process, an observer identifies the target lung nodule on patient's CT scans. Based on the identification, a volume of interest (VOI) containing the nodule is cropped from the entire CT volume and de-noised. Many noise reduction approaches are reported in the literature which could be applied according to the type of noise in the image [30]. The test CT images in our proposed method are enhanced by applying an anisotropic diffusion filter to the VOI. The application of anisotropic diffusion filter is known to preserve the nodule edges while eliminating the CT image noise [31]. Consequently, better edge based segmentation is obtained in medical CT

Table 1: Frequency distribution of sample nodules gray-values displayed in Figure 2

S. No	Mean radiodensity -630 HU		Mean radiodensity 10 HU		Mean radiodensity 100 HU	
	I_n	f_n	I_n	f_n	I_n	f_n
1.	39.85	51	74.25	306	74.1	430
2.	111.55	22	220.75	49	220.3	38
3.	183.25	9	367.25	36	366.5	26
4.	254.95	10	513.75	24	512.7	22
6.	326.65	4	660.25	27	658.9	10
6.	398.35	7	806.75	29	805.1	17
7.	470.05	22	953.25	228	951.3	283
8.	541.75	38	1099.8	183	1097.5	237
9.	613.45	30	1246.3	42	1243.7	70
10.	685.15	10	1392.8	6	1389.9	5

images. The anisotropic diffusion equation for an image $I(x, y)$ is given as [31]:

$$\frac{\partial I(x,y)}{\partial t} = div(C(x,y,t)\nabla I) \tag{12}$$

Here $C(x, y, t)$ is a conduction coefficient, ∇ is the gradient operator and div is the divergence operator. The conduction coefficient for edge persevering diffused image is defined as [31]:

$$C(x,y,t) = e^{-\frac{|\nabla I(x,y)|^2}{2K^2}} \tag{13}$$

Here K denotes a conductance parameter. The pre-processed images are shown to the observer who draws an elliptical region of interest (ROI) closely around the target nodule on a reference slice. Selection of VOI and ROI takes place through a customized computer interface. This practice sets a 3-D boundary beyond which the nodule cannot exist and minimizes the inclusion of vessels and other anatomical structures around the nodule. For the chosen ROI, the program computes the mean gray-level I_{mean} of target nodule using histogram-based technique presented in subsection 2.1.1 of the paper. The I_{mean} computation is followed by the execution of proposed system PDE in Eq. (9) in an iterative fashion. The iterative routine is stopped when an optimal 3-D nodule segmentation is achieved with a contour appearing around the target nodule.

Preprints (www.preprints.org) | NOT PEER-REVIEWED | Posted: 5 April 2019 doi:10.20944/preprints201904.0069.v1

Peer-reviewed version available at Elsevier Computers in Biology and Medicine 2018; doi:10.1016/j.compbiomed.2018.03.015

Algorithm 1:	
Input:	b, c, $\phi_t(k)$, I, I_{mean}, k, t, m
Step 1:	$\phi_t(k)$ is re-initialized to make $\|\phi\| = 1$
Step 2:	$\phi_t(k)$ is updated to $\widetilde{\phi_t(k)} = \phi_t(k) + \triangle t(c(I - I_{mean})$
Step 3:	$\widetilde{\phi_t(k)}$ is re-initialized to $\|\phi\| = 1$
Step 4:	$\widetilde{\phi_t(k)}$ is updated to $\phi_t(k+1) = \widetilde{\phi_t(k)} + \triangle t div(g(I)\nabla\phi)$
Step 5:	If $\phi_t(k+1)$ does not vary for m iterations or k exceeds a prescribed value, the routine is stopped resulting in optimal nodule segmentation otherwise control is transferred to Step 1.
Output :	3-D Segmentation

Further, any additional contours evolving around small vessels or structures within the ROI having a number of voxels less than 30 is removed. This particular value came from our observation that the smallest nodule has at least 30 voxels irrespective of the voxel size. The program counts the number of remaining contours if any, on each slice. If two or more objects are detected, the largest object which is supposedly the nodule is retained while the rest is removed. Figure 3 outlines the hybrid segmentation system architecture. It is worth noting that segmentation process becomes challenging with a large ROI selection having too many objects inside it or if the nodule of interest is not completely included in the ROI. Therefore, for an incorrect segmentation as per an expert's evaluation, the process of ROI selection and segmentation can be repeated. Finally, the volume of the nodule is the volume of one voxel times the total number of voxels contained in the segmented nodule.

3.4. Validation CT Databases

The experiments were performed by collecting test lung nodules from five different databases available at an open-access information resource for research purposes, The Cancer Imaging Archive (TCIA). Table 2 lists the number of nodules collected from each database with the corresponding slice thickness of CT volume. The resolution of test images is 512 x 512 pixels.

4. Results

The proposed framework is implemented in Matlab while level set re-initialization and AOS scheme are programmed in C++ language.

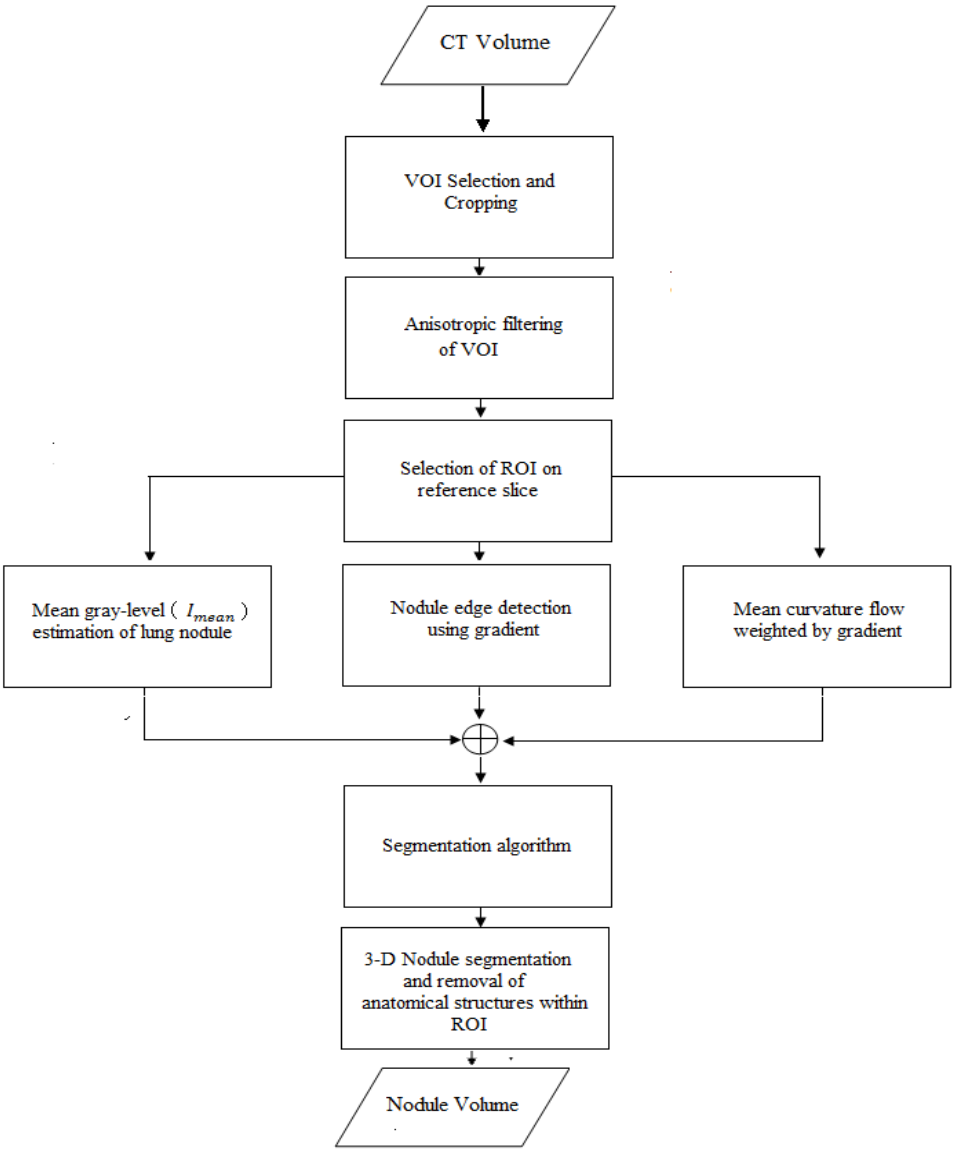

Figure 3: Hybrid System Architecture

System configuration is Intel Core Itanium 5 2430 M processor, 4 GB RAM memory, and 2.40 GHz clock. The parameters used in the algorithm execution are set to following optimal values: $b = 0.02$, $c = 0.001$, $t = 1$, $k = 25$, $p = 30$, $I_0 = 400$, Gaussian kernel dimensions = 5x5x5, $\sigma = 0.5$. Test CT collections comprise of lung nodules with diverse shapes and sizes and the median of estimated volumes varies in the order of 92 μl to 61.47 ml.

In Figure 4, we show a step by step execution of the proposed segmentation framework on a test nodule from the RIDER database with $\sigma = 0.5$, $\sigma = 0.3$ and $\sigma = 1$. The segmentation result achieved with $\sigma = 0.5$ is optimal among the three results obtained with different σ values as can be seen in Figure 4. To assess our proposed hybrid system, we compare its performance with two

Table 2: Nodules selection from validation CT Databases

Databases	Number of nodules scanned	Slice thickness range (mm)
CUMC[33]	12	1.25
RIDER[33]	10	1.25
FDA[34]	12	0.75
LIDC[35]	28	$1.0 - 2.5$
SU[36]	10	$0.625 - 1.25$

CUMC Columbia University Medical Center

RIDER Reference Image Database to evaluate Response Therapy

FDA Food and Drug Administration

LIDC Lung Imaging Database Consortium

SU Stanford University

well-known active contour models. First chosen model is classic Chan-Vese algorithm, a region based segmentation method which does not utilize object boundary information for segmentation. The curve evolution PDE of the model in level set form is given as follows in [32]:

$$\phi_t = -\delta(\phi)((I - c_1)^2 - (I - c_2)^2 - \mu\nabla.\frac{\nabla\phi}{|\nabla\phi|}) \tag{14}$$

Here I is the image function, ϕ is the level set function, $\delta(x)$ is the delta function and $\mu > 0$ is the length parameter chosen by the user. The constants c_1 and c_2 are updated at each iteration.

The second chosen model is local robust statistic driven active contour model by Gao et al. [37]. Curve evolution PDE of Gao et al. model for the closed contour $\phi_i(q,t)$ is given as :

$$\phi_t = [(1-\lambda)(p_i - (f(\phi_i(q,t))) - p^c) + k_i(q,t)].N_i(q,t) + S_i^{ext}(\phi_i(q,t)) \tag{15}$$

Here p_i is the probability density function of the feature space vectors $f(\phi_i(q,t))$, p^c is the cut off probability density fixed at 0.1, $\lambda > 0$ is the smoothness factor. N_i is the inward unit normal and k_i is the mean curvature for q which is spatial parameterization of the contour. With the intent of performance evaluation, we carried out manual segmentations of nodule data under the guidance of an expert radiologist to establish a ground truth. Segmentation and volume estimation using the Chan-Vese algorithm was performed on the Matlab platform whereas Slicer package [38] was employed to evaluate Gao et al. method.

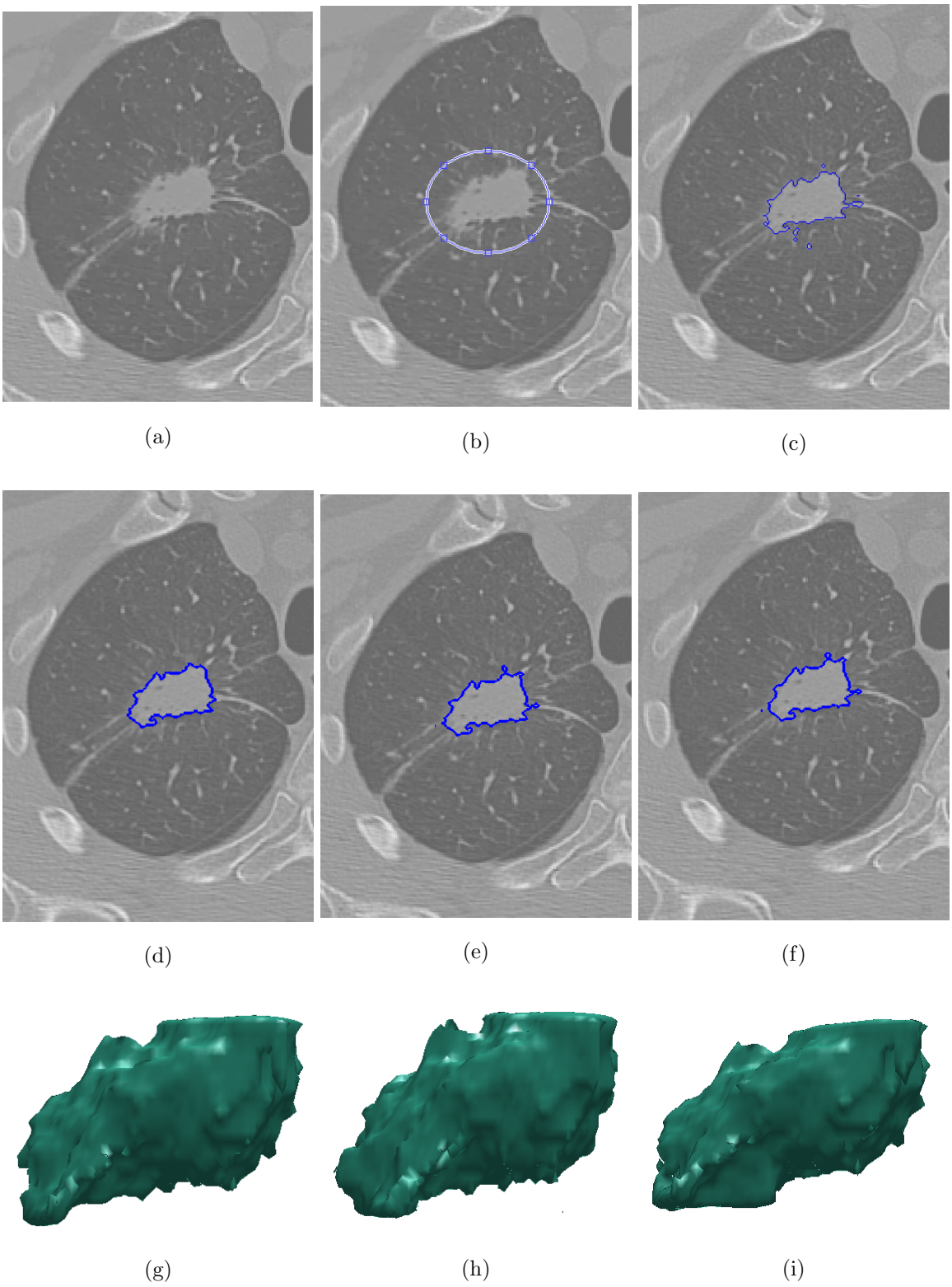

Figure 4: (a) shows reference slice of sample VOI from RIDER database (b) shows ROI selection on de-noised VOI (c) shows contours evolution within the ROI($\sigma = 0.5$) (d),(e),(f) show segmented nodule after undesirable contours removal with $\sigma = 0.5$(optimal), $\sigma = 0.3$ and $\sigma = 1$ respectively (g),(h),(i) show the surface areas of nodules in (d),(e) and (f) respectively

Peer-reviewed version available at Elsevier Computers in Biology and Medicine 2018; doi:10.1016/j.compbiomed.2018.03.015

For the comparison purpose, data sets were chosen from CUMC, FDA and LIDC databases since these have made available the true and estimated volumes of lung phantoms and lung nodules respectively. The shapes of the phantoms chosen for the experiment are lobulated, elliptical, spiculated and spherical as described by the CUMC and FDA phantom databases. Types of lung nodules selected from the LIDC database are well-circumscribed nodules, juxta-vascular nodules, and juxta-pleural nodules [15]. A well-circumscribed nodule is one which does not have any pulmonary structures or vessels attached. The nodule with vessels attached is termed as juxta-vascular nodule whereas, a nodule attached to the chest wall and the pleural surface is known as a juxta-pleural nodule.

4.1. Visual assessment of the segmentation system

In Figure 5, we show the segmentation of phantoms and their visualized surface areas using the Chan-Vese, Gao et al. and hybrid methods respectively. For lung nodule segmentation (nodule no. 580, no. 811, no. 965 from LIDC database), the results are presented in Figure 6.

We have a few observations after carrying out the visual comparison of three methods in Figure 5 and Figure 6. To begin with, the segmentation of lobulated, spherical, spiculated and elliptical nodule phantoms with the Chan-Vese method leads to contours leakage through the edges (Figure 5(a)). The algorithm uses two global terms c_{in} and c_{out} which work inside and outside of the object boundaries respectively to compute the location of contour. However, lack of gradient information produces poor results in well defined phantom segmentations in Figure 5(a). The evolved surface areas are over-estimated and the edges are oversmoothened resulting in a loss of actual nodule shape.

The second method from Gao et al. employs statistic features of a nodule for segmentation which includes intensity median, inter-quartile range and median absolute deviation computed in the neighborhood of each voxel. The resulting contours evolve around the nodule edges in an irregular manner whereas the obtained surface areas are rough and do not depict the exact shape of the phantom. This trend is more evident in the cases of elliptical, spherical and spiculated nodules, shown in Figure 5(b). In comparison, the proposed hybrid model has been able to evolve the contour as close to the edges as possible by utilizing region and boundary information, hence capturing the true shape of all the four phantoms in Figure 5(c). The deviation of contour from the nodules' edges is kept to a minimum.

Evaluating the performance on LIDC database, it is apparent from Figure 6(a) that Chan-Vese algorithm tends to over-segment juxta-pleural and juxta-vascular nodules leading to a slightly

enlarged respective surface areas. With Gao et al. method, the evolved surface area of well- circumscribed nodule does not represent the true nodule shape as shown in Figure 6(b). Moreover, the same method does not form a correct contour around juxta-pleural nodule (Figure 6(b)). The hybrid system, however successfully segments the well circumscribed and juxta-vascular nodules with correct surface areas formed whereas in the juxta-pleural nodule, there is a slight over-segmentation (Figure 6(c)). Comparing the overall performance, the hybrid system has segmented two nodules correctly whereas Gao et al. method and Chan-Vese method both segmented one each.

4.2. Quantitative assessment of the segmentation system

Quantitative performance of the system is measured in terms of volume bias, spatial overlap, and volume repeatability.

4.2.1. Volume bias

The volume bias of each of the three methods is estimated as the difference between computed volume and the true volume of phantoms [39]. Proportional bias is computed for the LIDC data sets available with the gold standard by applying Bland Altman method of 95 % limits of agreement [39].

A comparison of volume bias of all the three methods is plotted in Figure 7 for small phantoms (0.253 ml - 0.71 ml) and large phantom (4.21 ml - 4.44 ml) respectively. The bias of each method is found to differ with respect to the size of nodules as shown in Figure 7(a) and 7(b). All the three methods demonstrate an overall negative bias trend for small phantoms (Figure 7(a)). In case of large phantoms, Gao et al. method and hybrid system both show an equal tendency towards positive and negative bias whereas, the Chan-Vese method has a negative bias (Figure 7(b)). The computed absolute mean bias of the hybrid method, Gao et al. method, and the Chan-Vese method are 0.10 ± 0.2 ml, 0.19 ± 0.48 ml and 0.33 ± 0.21 ml respectively. Hence, the hybrid method shows the lowest mean bias among the three methods.

Bland Altman analysis with 95 % limits of agreement for the segmented volumes of LIDC datasets indicates an absolute mean bias of 0.09 ml, 0.4496 ml and 0.5674 ml for the hybrid method, Gao et al. method, and the Chan-Vese method respectively. Comparing the bias values, the hybrid method performs better on the LIDC test nodules.

Preprints (www.preprints.org) | NOT PEER-REVIEWED | Posted: 5 April 2019 doi:10.20944/preprints201904.0069.v1

Peer-reviewed version available at Elsevier Computers in Biology and Medicine 2018; doi:10.1016/j.compbiomed.2018.03.015

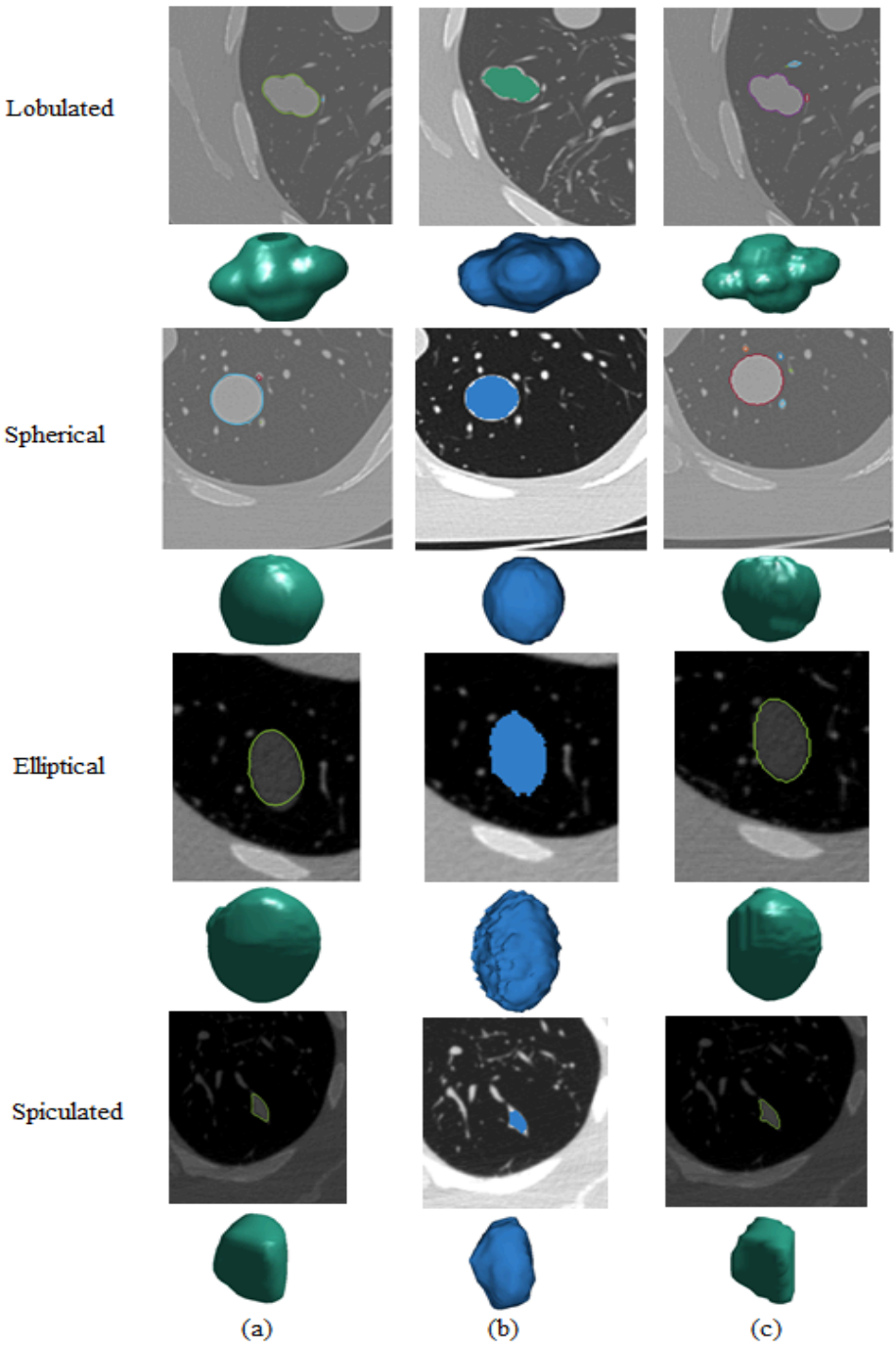

Figure 5: Segmentation of lobulated, spherical, elliptical and spiculated phantoms from CUMC and FDA database and their visualized surface area using (a) Chan-Vese method (b) Gao et al. method (c) Hybrid method

Preprints (www.preprints.org) | NOT PEER-REVIEWED | Posted: 5 April 2019 doi:10.20944/preprints201904.0069.v1

Peer-reviewed version available at *Elsevier Computers in Biology and Medicine* **2018**; doi:10.1016/j.compbiomed.2018.03.015

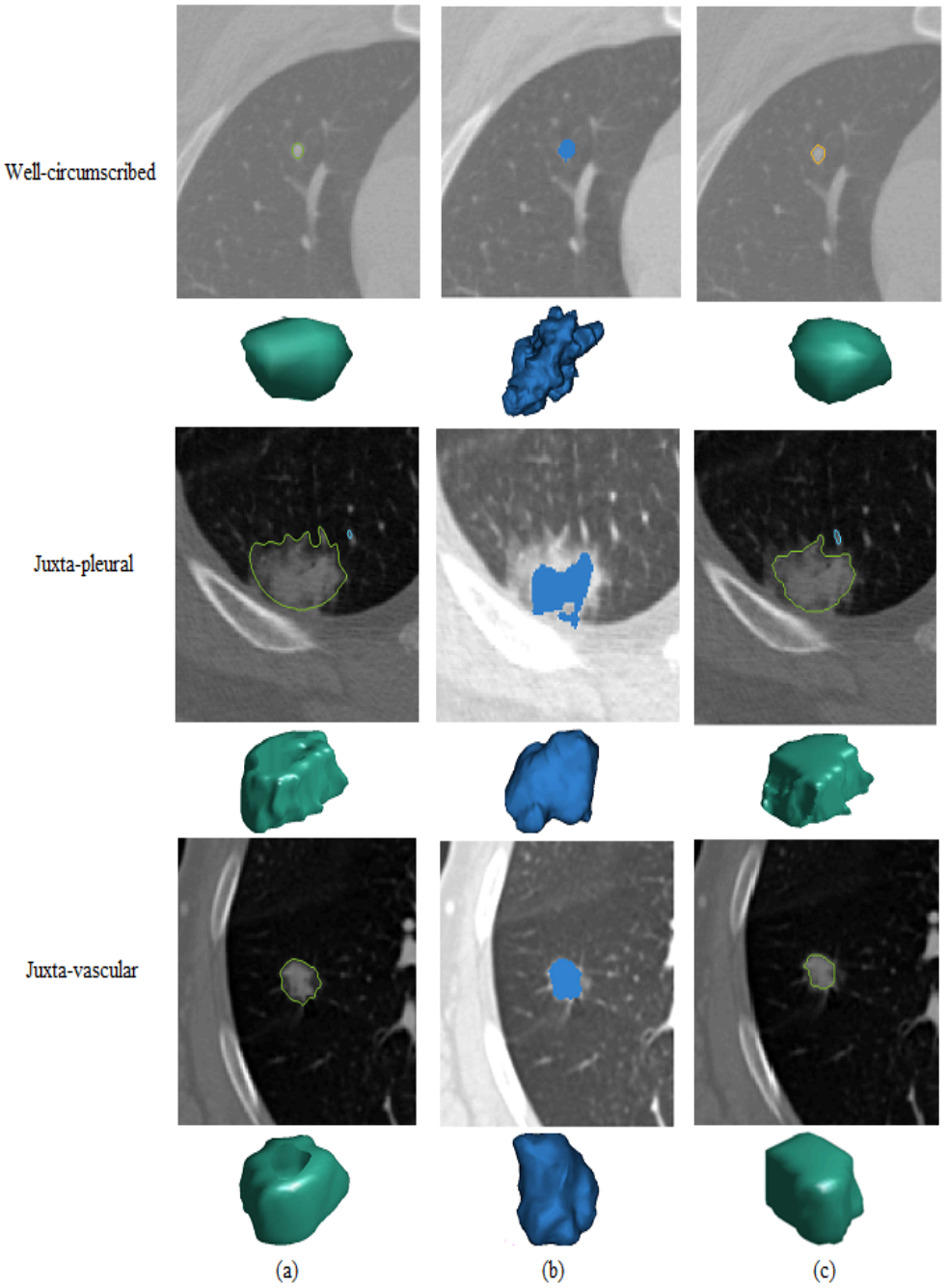

Figure 6: Segmentation of well-circumscribed (nodule no. 580), juxta-pleural nodule (nodule no. 811) and juxta-vascular (nodule no. 965) from LIDC database and their visualized surface areas using (a) Chan-Vese method (b) Gao et al. method (c) Hybrid method

Table 3: Segmentation performance scores

Parameter	Formula	Mean Score
F1 Score	$\frac{2(GS)}{(GS+GS)}$	0.8569 ± 0.0431
TPR	$\frac{TP}{TP+FN}$	0.87
FPR	$\frac{FP}{FP+TN}$	0.05

4.2.2. Similarity Measure

In addition to comparative analysis, we also evaluate the hybrid system independently on our chosen validation databases. Dice coefficient DC, also known as the F1 score is employed to measure the extent of spatial overlap between the ground truth binary image G and the segmented binary image S. True Positive Rate(TPR) and False Positive Rate(FPR) scores are computed to further assess the quality of segmentation. We report the obtained mean values in Table 3. The True Positive(TP) value denote voxels segmented as a nodule that proved to be nodule and False Positive(FP) denotes voxels segmented as a nodule that proved to be non-nodule. The False Negative(FN) value represents voxels segmented as a non-nodule that proved to be nodule and True Negative(TN) represents voxels segmented as a non- nodule that proved to be non-nodule.

The algorithm produces a mean $DC/F1$ value of 0.8569 ± 0.0431 whereas, the mean TPR and FPR scores are 0.87 and 0.05 respectively which attribute to the good performance of the algorithm.

4.2.3. Volume Repeatability

Next, we compute the volume repeatability of algorithm by taking three repeated volume measurements of every test nodule. The Repeatability Coefficient (RC) measures the difference between the repeated volume measurements under identical set of conditions for 95 % confidence interval as follows [39]:

$$RC = 1.96\sqrt{2s_w^2} \tag{16}$$

Here s_w^2 is the within-subject variance. The second parameter, the within-subject Coefficient of Variation measures the changes within repeated measurements and is given in [39] as:

$$wCV = \frac{s_w}{\mu} \tag{17}$$

Preprints (www.preprints.org) | NOT PEER-REVIEWED | Posted: 5 April 2019 doi:10.20944/preprints201904.0069.v1

Peer-reviewed version available at *Elsevier Computers in Biology and Medicine* **2018**; doi:10.1016/j.compbiomed.2018.03.015

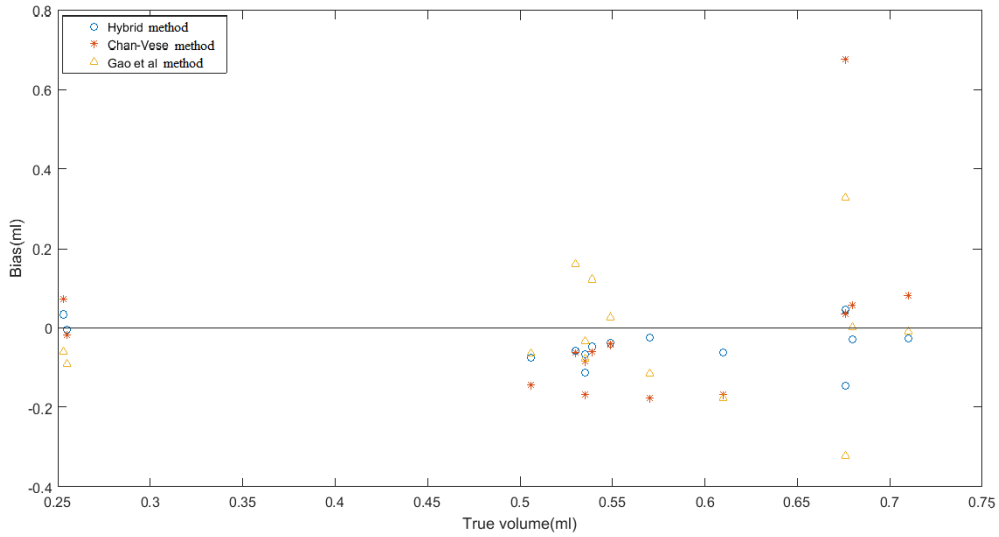

(a)

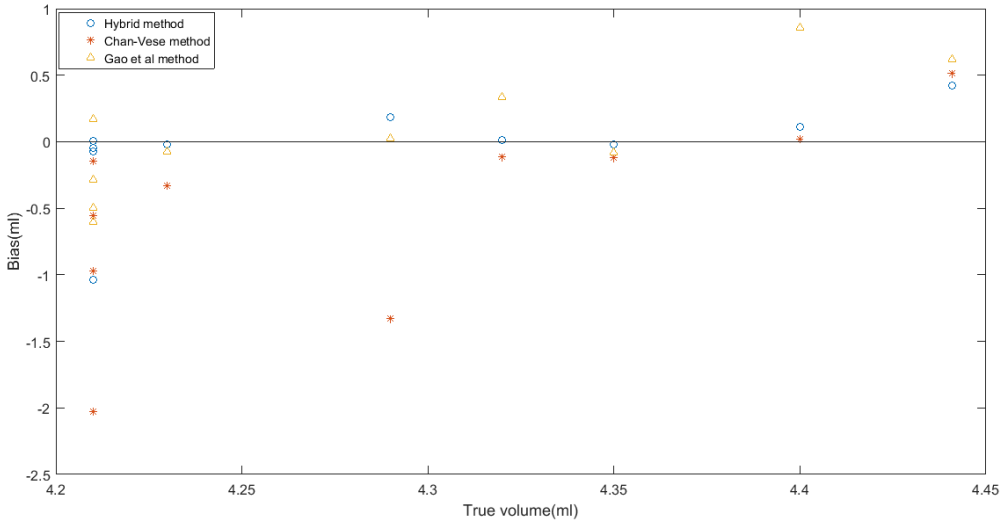

(b)

Figure 7: Comparison of estimated volume bias of three methods for (a)small phantoms (b)large phantoms

Table 4: Repeatability results of hybrid system

$RC(ml)$	wCV	CCC (95% confidence interval)
0.060	0.152%	$0.9981(0.9970 - 0.9988)$

RC	Repeatability Coefficient
wCV	Within-subject Coefficient of Variance
CCC	Concordance Correlation Coefficient

Here μ is the mean of measured outcomes. Further, Concordance Correlation Coefficient (CCC) evaluates the agreement of repeated outcomes with respect to the total variation in the observations [39]. A total of 72 x 3 = 216 segmentations were carried out to compute the values of RC , wCV and CCC. The results are reported in Table 4. The algorithm is repeatable by 0.060 ml and the variance within-subject is 0.152%. A high CCC value of 0.9981 is obtained with 95 % confidence interval.

5. Discussion

It is important to emphasize the careful selection of ROI geometry for correct nodule segmentation. This is particularly true for nodules with dark contrast and in-homogeneous intensity values. We assess the impact of ROI geometry on our method by varying the ROI size for the aforementioned challenging segmentation scenarios. Figure 8(a) and 8(b) show small and large ROI initialization respectively around a low-intensity nodule and the corresponding segmentation results are shown in Figure 8(e) and 8(f) respectively. Similar ROI selections around a nodule with intensity inhomogeneity are presented in Figure 8(c) and 8(d), and the corresponding segmentations are demonstrated in Figure 8(g) and 8(h) respectively. The results show successful segmentation of low-intensity nodule irrespective of the ROI size. However, a contour leakage occurs when a large ROI is initialized around the intensity inhomogeneous nodule in Figure 8(h). This could be expected due to the presence of I_{mean} variable as a stopping function in the hybrid PDE. Therefore, small contour initialization leads to optimal segmentation and is the preferred choice for our method. Our system has segmented 68 nodules correctly and failed on two juxta-pleural nodules, one dark contrast nodule, and two juxta-vascular nodules leading to 93% correct segmentation.

The efficacy of a 3-D segmentation algorithm should be ideally evaluated against standard databases with available ground truth in order to develop a consensus for benchmarking. Unfor-

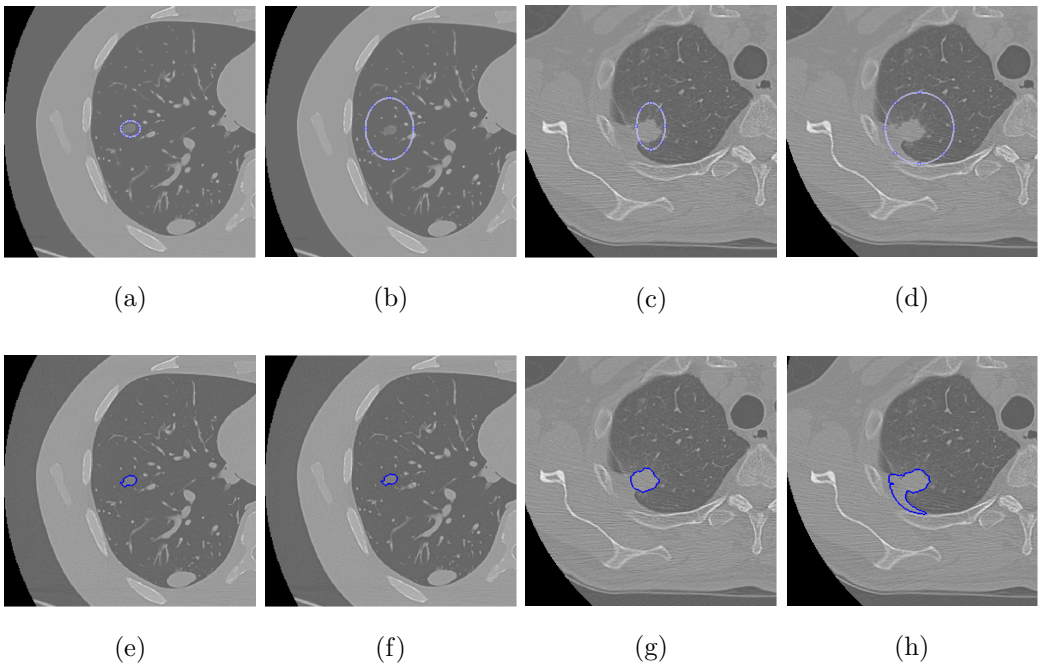

Figure 8: (a),(b) show small and large ROI initialization around a low intensity nodule (c),(d) show small and large ROI initialization around a nodule with intensity inhomogeneity (e),(f),(g),(h) show segmentation results of (a),(b),(c) and (d) respectively

tunately, many good segmentation methods in the literature assessed their performance on private databases making it difficult to draw a comparison. During the last decade however, LIDC database has emerged as a standard and is widely used for segmentation algorithms evaluation. Therefore, we assess the efficacy of our proposed work by comparing the hybrid segmentation method with the best segmentation schemes,new as well as classic with their results published on LIDC database in Table 5.

We observe that with Diciotti et al.'s[17] work as an exception, all the other proposed methods including Badura et al.[40], Kubota et al.[41], Messay et al.[21], Wang et al.[42] and Goncalves et al.[43] evaluated special overlap as a key performance indicator. With the intent of comprehensive performance analysis, we compute the spatial overlap as well as the volume bias. The hybrid method achieves a spatial overlap of 0.82 on LIDC database which is a significantly higher value than the reported aforementioned studies. Comparison of the volume bias value could not be made possible due to its absence in the chosen published studies.

It is noteworthy that prominent 3-D nodule segmentation methods in the literature have not considered qualitative nodule shape assessment a part of the performance metric. While Diciotti et

Table 5: Segmentation performance comparison with existing algorithms on LIDC data sets

Article	Databases	Mean spatial overlap	Mean volume bias	3-D visual analysis
P. Badura [40]	LIDC	0.6 ± 0.16	-	No
Kubota et al. [41]	LIDC	0.69 ± 0.18	-	No
Diciotti et al. [17]	LIDC	-	-	No
Hybrid method	LIDC	0.82± 0.08	0.09 ml	Yes
Messay et al. [21]	LIDC	0.778 ± 0.863	-	No
Wang et al. [42]	LIDC	0.64	-	No
Goncalves et al. [43]	LIDC	0.64	-	No

al.[44] used shape assessment for nodule segmentation, El-Baz et al.[45] and Krishnamurthy et al.[46] employed the shape analysis for lung cancer diagnosis. Therefore, an important contribution of our work in terms of performance analysis is the inclusion of the 3-D visual assessment of segmented nodules. In this respect, our work can be considered original and the first attempt towards 3-D qualitative analysis of the test data-sets.

Based on the quantitative and visual comparative analysis presented in the paper, the hybrid system clearly stands out from segmentation methods by Gao et al. and Chan-Vese. It is capable of performing accurate segmentation on small as well as on large nodules, and demonstrated a mean spatial overlap of 85.6 % and mean TPR and FPR as 88% and 5% respectively. Moreover, the presented method is highly reproducible with a CCC of 0.99. The achieved results showcase the accuracy, robustness, and stability of the system. One of the future avenues to increase the efficiency of the proposed method is to improvise on the I_{mean} calculation method to address the low-intensity problem within the near-end slices. Another possible direction for future research work is to implement the presented hybrid level set evolution using Sobolev gradient [47][48] and to evaluate it against our existing implementation of the steepest descent gradient method.

6. Conclusion

We have proposed an accurate, flexible and stable semi-automatic system for lung nodule segmentation in this paper. The aim of the presented method is to increase the accuracy of segmentation by exploiting both, the region as well as the boundary information of the nodule in a

CT image. Our technique has successfully addressed the boundary leakage problem along with over-segmentation and under-segmentation issue which is supposedly a problem area in otherwise preferred region growing techniques. We tested the algorithm on small as well as large-sized lung nodules from various validation databases and have obtained good segmentation results in terms of bias, spatial overlap and repeatability. The results indicate that the proposed approach is a needed step towards accurate nodule segmentation through hybrid deformable models.

Acknowledgement

The authors acknowledge all the contributors who made the lung CT datasets publicly available on TCIA site. The authors would also like to thank Dr. Tahir Qasim, from NUCES for his valuable suggestions towards the improvement of this research paper.

References

[1] J. Didkowska, U. Wojciechowska, M. Manczuk, J. Lobaszewski, and et al, "Lung cancer epidemiology: Contemporary and future challenges worldwide," *Annals of Translational Medicine*, vol. 4, no. 8, 2016, ISSN: 2305-5847. [Online]. Available: http://atm.amegroups.com/article/view/9532.

[2] M. Firmino, G. Angelo, H. Morais, M. R. Dantas, and R. Valentim, "Computer-aided detection (cade) and diagnosis (cadx) system for lung cancer with likelihood of malignancy," *BioMedical Engineering OnLine*, vol. 15, no. 1, p. 2, Jan. 2016, ISSN: 1475-925X. DOI: 10.1186/s12938-015-0120-7. [Online]. Available: https://doi.org/10.1186/s12938-015-0120-7.

[3] J. K. Field, "Uk lung cancer rct pilot screening trial: Baseline findings from the screening arm provide evidence for the potential implementation of lung cancer screening," *Thorax*, vol. 71, no. 2, pp. 161–170, 2016, ISSN: 0040-6376. DOI: 10.1136/thoraxjnl-2015-207140. eprint: http://thorax.bmj.com/content/71/2/161.full.pdf. [Online]. Available: http://thorax.bmj.com/content/71/2/161.

[4] N. Horeweg, E. T. Scholten, and P. D. Jong, "Detection of lung cancer through low-dose ct screening (nelson): A prespecified analysis of screening test performance and interval cancers," *The Lancet Oncology*, vol. 15, 2014.

[5] P. D. Mozley, C. Bendtsen, B. Zhao, L. H.Schwartz, M. Thorn, Y. Rong, L. Zhang, A. Perrone, ReneKorn, and A. J.Buckler, "Measurement of tumor volumes improves recist-based response assessments in advanced lung cancer," *Translational Oncology.*, vol. 5, pp. 19–25, 2012.

[6] M. Becker and M.-. Thalmann, *Deformable models in medical image segmentation:, 3D multiscale physiological human*. Springer London, 2014, pp. 81–106.

[7] Y. Kawata, N. Niki, H. Ohmatsu, and N. Moriyama, "A deformable surface model based on boundary and region information for pulmonary nodule segmentation from 3-d thoracic ct images," *IEICE TRANSACTIONS on Information and Systems*, pp. 1921–1930, 2003.

[8] A. El-Baz, A. Farag, G. Gimel'farb, R. Falk, M. A. El-Ghar, and T. Eldiasty, "A framework for automatic segmentation of lung nodules from low dose chest ct scans," in *18th International Conference on Pattern Recognition (ICPR'06)*, vol. 3, 2006, pp. 611–614. DOI: 10.1109/ICPR.2006.66.

[9] Y. Yongseok, S. Hackjoon, Y. Dong, W. L. Kyung, and U. L. Sang, "Segmentation of ground glass opacities by asymmetric multi-phase deformable model," in *Medical Imaging: Image Processing,Proc.SPIE*, 2006. [Online]. Available: http://dx.doi.org/10.1117/12.653053.

[10] T. Way, L. Hadjiiski, B. S. B, H. Chan, P. Cascade, E. Kazerooni, N. Bogot, and C. Zhou, "Computer-aided diagnosis of pulmonary nodules on ct scans: Segmentation and classification using 3d active contours," *Medical Physics*, vol. 33, no. 7Part1, pp. 2323–2337, 2006, ISSN: 2473-4209. DOI: 10.1118/1.2207129. [Online]. Available: http://dx.doi.org/10.1118/1.2207129.

[11] K. chen, B. Li, L. Tian, W. Zhu, and Y. Bao, "Fuzzy speed function based active contour model for segmentation of pulmonary nodules," in *Frontiers in Biomedical Engineering and Biotechnology ,Proceedings of the 2nd International Conference on Biomedical Engineering and Biotechnology*, 2013.

[12] B. Li, Q. Chen, G. Peng, Y. Guo, K. Chen, L. Tian, S. Ou, and L. Wang, "Segmentation of pulmonary nodules using adaptive local region energy with probability density function-based similarity distance and multi-features clustering," *BioMedical Engineering OnLine*, vol. 15, no. 1, p. 49, May 2016, ISSN: 1475-925X. DOI: 10.1186/s12938-016-0164-3. [Online]. Available: https://doi.org/10.1186/s12938-016-0164-3.

[13] M. Firmino, A. H. Morais, R. Mendoca, M. R. Dantas, H. R. Hekis, and R. Valentim, "Computer-aided detection system for lung cancer in computed tomography scans: Review and future prospects," *BioMedical Engineering OnLine*, vol. 13, no. 1, p. 41, Apr. 2014, ISSN: 1475-925X. DOI: 10.1186/1475-925X-13-41. [Online]. Available: https://doi.org/10.1186/1475-925X-13-41.

[14] A. El-Baz, G. M. Beache, G. Gimel'farb, K. Suzuki, K. Okada, A. Elnakib, A. Soliman, and B. Abdollahi, "Computer-aided diagnosis systems for lung cancer: Challenges and methodologies," in *International Journal of Biomedical Imaging*, 2013.

[15] W. J. Kostis, A. P. Reeves, D. F. Yankelevitz, and C. I. Henschke, "Three-dimensional segmentation and growth-rate estimation of small pulmonary nodules in helical ct images," *IEEE Transactions on Medical Imaging*, vol. 22, no. 10, pp. 1259–1274, Oct. 2003, ISSN: 0278-0062. DOI: 10.1109/TMI.2003.817785.

[16] K. Okada, D. Comaniciu, and A. Krishnan, "Robust anisotropic gaussian fitting for volumetric characterization of pulmonary nodules in multislice ct," *IEEE Transactions on Medical Imaging*, vol. 24, no. 3, pp. 409–423, Mar. 2005, ISSN: 0278-0062. DOI: 10.1109/TMI.2004.843172.

[17] S. Diciotti, G. Picozzi, M. Falchini, M. Mascalchi, N. Villari, and G. Valli, "3-d segmentation algorithm of small lung nodules in spiral ct images," *IEEE Transactions on Information Technology in Biomedicine*, vol. 12, no. 1, pp. 7–19, Jan. 2008, ISSN: 1089-7771. DOI: 10.1109/TITB.2007.899504.

[18] J. M. Kuhnigk, V. Dicken, L. Bornemann, A. Bakai, D. Wormanns, S. Krass, and H. O. Peitgen, "Morphological segmentation and partial volume analysis for volumetry of solid pulmonary lesions in thoracic ct scans," *IEEE Transactions on Medical Imaging*, vol. 25, no. 4, pp. 417–434, Apr. 2006, ISSN: 0278-0062. DOI: 10.1109/TMI.2006.871547.

[19] J. H. Moltz, L. Bornemann, J.-M. Kuhnigk, V. Dicken, E. Peitgen, S. Meier, H. Bolte, M. Fabel, H.-C. Bauknecht, M. Hittinger, Andreas, M. Pusken, and H.-O. Peitgen, "Advanced segmentation techniques for lung nodules, liver metastases, and enlarged lymph nodes in ct scans," *IEEE Journal of Selected Topics in Signal Processing*, vol. 3, no. 1, pp. 122–134, Feb. 2009, ISSN: 1932-4553. DOI: 10.1109/JSTSP.2008.2011107.

[20] C. Bendtsen, M. Kietzmann, R. Korn, P. D. Mozley, G. Schmidt, and G. Binnig, "X-ray computed tomography: Semiautomated volumetric analysis of late-stage lung tumors as a basis for response assessments," *Journal of Biomedical Imaging*, vol. 2011, 5:1–5:11, Jan.

2011, ISSN: 1687-4188. DOI: 10.1155/2011/361589. [Online]. Available: http://dx.doi.org/10.1155/2011/361589.

[21] T. Messay, R. C. Hardie, and T. R. Tuinstra, "Segmentation of pulmonary nodules in computed tomography using a regression neural network approach and its application to the lung image database consortium and image database resource initiative dataset," *Medical Image Analysis*, vol. 22, no. 1, pp. 48–62, 2015, ISSN: 1361-8415. DOI: https://doi.org/10.1016/j.media.2015.02.002. [Online]. Available: http://www.sciencedirect.com/science/article/pii/S1361841515000316.

[22] V. Caselles, F. Catte, and T. Coll, "A geometric model for active contours in image processing," *Numer. Math.*, vol. 66, pp. 1–31, 1993.

[23] A. Khadidos, V. Sanchez, and C. T. Li, "Weighted level set evolution based on local edge features for medical image segmentation," *IEEE Transactions on Image Processing*, vol. 26, no. 4, pp. 1979–1991, Apr. 2017, ISSN: 1057-7149. DOI: 10.1109/TIP.2017.2666042.

[24] E. Goceri, "Fully automated liver segmentation using sobolev gradient-based level set evolution," *International Journal for Numerical Methods in Biomedical Engineering*, vol. 32, no. 11, e02765–n/a, 2016, e02765 CNM-Jun-15-0095.R1, ISSN: 2040-7947. DOI: 10.1002/cnm.2765. [Online]. Available: http://dx.doi.org/10.1002/cnm.2765.

[25] P. Swierczynski, B. W. Papiez, J. A. Schnabel, and C. Macdonald, "A level-set approach to joint image segmentation and registration with application to ct lung imaging," *Computerized Medical Imaging and Graphics*, 2017, ISSN: 0895-6111. DOI: https://doi.org/10.1016/j.compmedimag.2017.06.003. [Online]. Available: http://www.sciencedirect.com/science/article/pii/S0895611117300526.

[26] E. Goceri, M. Z. Unlu, and O. Dicle, "A comparative performance evaluation of various approaches for liver segmentation from spir images," *Turk J Elec Eng Comp Sci*, vol. 23, no. 3, pp. 741–768, 2015, ISSN: 1303-6203.

[27] S. Osher and J. A. Sethian, "Fronts propagating with curvature-dependent speed: Algorithms based on hamilton-jacobi formulations," *Journal of Computational Physics*, vol. 79, no. 1, pp. 12–49, 1988, ISSN: 0021-9991. DOI: https://doi.org/10.1016/0021-9991(88)90002-2. [Online]. Available: http://www.sciencedirect.com/science/article/pii/0021999188900022.

[28] N. R. Morgan and J. I. Waltz, "3d level set methods for evolving fronts on tetrahedral meshes with adaptive mesh refinement," *Journal of Computational Physics*, vol. 336, no. Supplement C, pp. 492–512, 2017, ISSN: 0021-9991. DOI: https://doi.org/10.1016/j.jcp.2017.02.030. [Online]. Available: http://www.sciencedirect.com/science/article/pii/S0021999117301237.

[29] J. H. Kim, B.-Y. Park, F. Akram, B.-W. Hong, and K. N. Choi, "Multipass active contours for an adaptive contour map," *Sensors*, vol. 13, pp. 3724–3738, 2013.

[30] E. Goceri, B. Goksel, J. W. Elder, V. K. Puduvalli, J. J. Otero, and M. N. Gurcan, "Quantitative validation of anti-ptbp1 antibody for diagnostic neuropathology use: Image analysis approach," *International Journal for Numerical Methods in Biomedical Engineering*, vol. 33, no. 11, e2862–n/a, 2017, e2862 CNM-Oct-16-0231.R1, ISSN: 2040-7947. DOI: 10.1002/cnm.2862. [Online]. Available: http://dx.doi.org/10.1002/cnm.2862.

[31] K. Suzuki, H. T. Huynh, Y. Liu, D. Calabrese, K. Zhou, A. Oto, and M. Hori, "Computerized segmentation of liver in hepatic ct and mri by means of level-set geodesic active contouring," in *2013 35th Annual International Conference of the IEEE Engineering in Medicine and Biology Society (EMBC)*, Jul. 2013, pp. 2984–2987. DOI: 10.1109/EMBC.2013.6610167.

[32] T. F. Chan and L. A. Vese, "Active contours without edges," *IEEE Transactions on Image Processing*, vol. 10, no. 2, pp. 266–277, Feb. 2001, ISSN: 1057-7149. DOI: 10.1109/83.902291.

[33] B. Zhao, L. James, C. Moskowitz, P. Guo, M. Ginsberg, R. Lefkowitz, Y. Qin, G. Riely, M. Kris, and L. Schwartz, "Evaluating variability in tumor measurements from same-day repeat ct scans of patients with non-small cell lung cancer," *Radiology*, vol. 252, no. 1, pp. 263–272, 2009, PMID: 19561260. eprint: https://doi.org/10.1148/radiol.2522081593. [Online]. Available: https://doi.org/10.1148/radiol.2522081593.

[34] M. A. Gavrielides, L. M. Kinnard, K. J. Myers, J. Peregoy, W. F. Pritchard, R. Zeng, J. Esparza, J. Karanian, and N. Petrick, "A resource for the assessment of lung nodule size estimation methods: Database of thoracic ct scans of an anthropomorphic phantom," *Opt. Express*, vol. 18, no. 14, pp. 15 244–15 255, Jul. 2010. DOI: 10.1364/OE.18.015244. [Online]. Available: http://www.opticsexpress.org/abstract.cfm?URI=oe-18-14-15244.

[35] S. Armato and et al., "The lung image database consortium (lidc) and image database resource initiative (idri): A completed reference database of lung nodules on ct scans," *Medical*

Physics, vol. 38, no. 2, pp. 915–931, 2011, ISSN: 2473-4209. DOI: 10.1118/1.3528204. [Online]. Available: http://dx.doi.org/10.1118/1.3528204.

[36] O. Gevaert, J. Xu, C. D. Hoang, A. N. Leung, Y. Xu, A. Quon, D. L. Rubin, S. Napel, and S. K. Plevritis, "Non-small cell lung cancer: Identifying prognostic imaging biomarkers by leveraging public gene expression microarray data -methods and preliminary results," *Radiology*, vol. 264, no. 2, pp. 387–396, 2012, PMID: 22723499. DOI: 10.1148/radiol.12111607. eprint: https://doi.org/10.1148/radiol.12111607. [Online]. Available: https://doi.org/10.1148/radiol.12111607.

[37] Y. Gao, R. Kikinisb, and A. T. Sylvain Bouixa Martha Shentona, "A 3d interactive multi-object segmentation tool using local robust statistics driven active contours," *Medical Image Analysis*, vol. 16, pp. 1216–1227, 2012.

[38] A. Fedorov, "3d slicer as an image computing platform for the quantitative imaging network," *Magnetic resonance imaging*, vol. 9, pp. 1323–1341, 2012.

[39] J. Kalpathy-Cramer, B. Zhao, D. Goldgof, Y. Gu, X. Wang, H. Yang, Y. Tan, R. Gillies, and S. Napel, "A comparison of lung nodule segmentation algorithms: Methods and results from a multi-institutional study," *Journal of Digital Imaging*, vol. 29, no. 4, pp. 476–487, Aug. 2016, ISSN: 1618-727X. DOI: 10.1007/s10278-016-9859-z. [Online]. Available: https://doi.org/10.1007/s10278-016-9859-z.

[40] P. Badura and E. Pietka, "Soft computing approach to 3d lung nodule segmentation in ct," *Computers in Biology and Medicine*, vol. 53, no. Supplement C, pp. 230–243, 2014, ISSN: 0010-4825. DOI: https://doi.org/10.1016/j.compbiomed.2014.08.005. [Online]. Available: http://www.sciencedirect.com/science/article/pii/S0010482514002078.

[41] T. Kubota, A. Jerebko, M. Salganicoff, M. Dewan, and A. Krishnan, "Segmentation of pulmonary nodules of various densities with morphological approaches and convexity models," *Medical Image Analysis*, vol. 15, pp. 133–154, 2008.

[42] J. Wang, R. Engelmann, and Q. Li, "Segmentation of pulmonary nodules in three-dimensional ct images by use of a spiral-scanning technique," *Medical Physics*, vol. 34, no. 12, pp. 4678–4689, 2007, ISSN: 2473-4209. DOI: 10.1118/1.2799885. [Online]. Available: http://dx.doi.org/10.1118/1.2799885.

[43] L. Gonasalves, J. Novo, and A. Campilho, "Hessian based approaches for 3d lung nodule segmentation," *Expert Systems with Applications*, vol. 61, pp. 1–15, 2016, ISSN: 0957-4174. DOI: https://doi.org/10.1016/j.eswa.2016.05.024. [Online]. Available: http://www.sciencedirect.com/science/article/pii/S0957417416302494.

[44] S. Diciotti, S. Lombardo, M. Falchini, G. Picozzi, and M. Mascalchi, "Automated segmentation refinement of small lung nodules in ct scans by local shape analysis," *IEEE Transactions on Biomedical Engineering*, vol. 58, no. 12, pp. 3418–3428, Dec. 2011, ISSN: 0018-9294. DOI: 10.1109/TBME.2011.2167621.

[45] A. El-Baz, M. Nitzken, F. Khalifa, A. Elnakib, G. Gimel'farb, R. Falk, and M. A. El-Ghar, "3d shape analysis for early diagnosis of malignant lung nodules," in *Information Processing in Medical Imaging*, G. Székely and H. K. Hahn, Eds., Berlin, Heidelberg: Springer Berlin Heidelberg, 2011, pp. 772–783, ISBN: 978-3-642-22092-0.

[46] S. Krishnamurthy, G. Narasimhan, and U. Rengasamy, "Three-dimensional lung nodule segmentation and shape variance analysis to detect lung cancer with reduced false positives," *Proceedings of the Institution of Mechanical Engineers, Part H: Journal of Engineering in Medicine*, vol. 230, no. 1, pp. 58–70, 2016, PMID: 26721427. DOI: 10.1177/0954411915619951. eprint: https://doi.org/10.1177/0954411915619951. [Online]. Available: https://doi.org/10.1177/0954411915619951.

[47] E. Goceri, "Effects of chosen scalar products on gradient descent algorithms," in *The 28th International Conference of The Jangjeon Mathematical Society ICJMS 2015*, 5-19 May 2015, pp.90–90.

[48] J. A. Hatton, "Using gradient descent method to solve systems of differential equations under the sobolev inner product space," PhD thesis, Lamar University, 2017.